minerals

MDPI

Article

Quantification of Kaolinite and Halloysite Using Machine Learning from FTIR, XRF, and Brightness Data

Pieter I. Du Plessis [1], Michael F. Gazley [2,3,*], Stephanie L. Tay [2], Eliza F. Trunfull [4], Manuel Knorsch [4], Thomas Branch [4] and Louis F. Fourie [5]

[1] DataPLP, P.O. Box 8461, Saskatoon, SK S7K 6K5, Canada; pieter.duplessis@terramodellingservices.ca
[2] RSC, Level 2, 93 The Terrace, Wellington 6011, New Zealand; s.tay@rscmme.com
[3] School of Geography, Environment and Earth Science, Victoria University of Wellington, Wellington 6012, New Zealand
[4] RSC, 45 Ventnor Ave, West Perth, WA 6005, Australia; e.trunfull@rscmme.com (E.F.T.); m.knorsch@rscmme.com (M.K.); t.branch@rscmme.com (T.B.)
[5] Terra Modelling Services Inc., P.O. Box 8461, Saskatoon, SK S7K 6K5, Canada; l.fourie@rscmme.com
* Correspondence: m.gazley@rscmme.com

Abstract: Quantification of halloysite and kaolinite in clay deposits from X-ray diffraction (XRD) commonly requires extensive sample preparation to differentiate the two phyllosilicates. When assessing hundreds of samples for mineral resource estimations, XRD analyses may become unfeasible due to time and expense. Fourier transform infrared (FTIR) analysis is a fast and cost-effective method to discriminate between kaolinite and halloysite; however, few efforts have been made to use this technique for quantified analysis of these minerals. In this study, we trained machine- and deep-learning models on XRD data to predict the abundance of kaolinite and halloysite from FTIR, chemical composition, and brightness data. The case study is from the Cloud Nine kaolinite–halloysite deposit, Noombenberry Project, Western Australia. The residual clay deposit is hosted in the saprolitic and transition zone of the weathering profile above the basement granite on the south-western portion of the Archean Yilgarn Craton. Compared with XRD quantification, the predicted models have an R^2 of 0.97 for kaolinite and 0.96 for halloysite, demonstrating an excellent fit. Based on these results, we demonstrate that our methodology provides a cost-effective alternative to XRD to quantify kaolinite and halloysite abundances.

Keywords: kaolin; clay; machine learning; deep learning; quantification; XRD

Citation: Du Plessis, P.I.; Gazley, M.F.; Tay, S.L.; Trunfull, E.F.; Knorsch, M.; Branch, T.; Fourie, L.F. Quantification of Kaolinite and Halloysite Using Machine Learning from FTIR, XRF, and Brightness Data. *Minerals* **2021**, *11*, 1350. https://doi.org/10.3390/min11121350

Academic Editor: Stephen Hillier

Received: 29 October 2021
Accepted: 29 November 2021
Published: 30 November 2021

1. Introduction

A mineral resource estimate was recently completed on the Cloud Nine kaolinite–halloysite deposit, part of the Noombenberry Project in Western Australia. The quantification of kaolinite and halloysite (the two main clay minerals present at Noombenberry) and other minerals within the project was completed using X-ray diffraction (XRD). This is an expensive and labour-intensive technique for mineral quantification. Differentiating halloysite from kaolinite can require chemical and physical treatment prior to the XRD analysis [1]. The intercalation of organic molecules into halloysite results in increased spacing between the silicate layers, which in turn shifts the peak positions on the XRD patterns. Small quantities of halloysite are challenging to detect in kaolinite-rich samples due to overlapping peaks in XRD patterns [2].

Alongside the XRD dataset, Fourier transform infrared (FTIR) data were also collected on the same samples. The FTIR technique requires minimal sample preparation and is more cost and time effective than XRD. Coupled with machine learning (ML) approaches, FTIR data have been used for mineral identification and to predict parameters such as elemental abundance, grain size, density, total organic carbon, pH, and other properties of soils and rocks [3–12]. While FTIR is commonly employed to analyse these physicochemical

parameters, it is less commonly applied in the quantification of mineral abundances. Yet, the individual intensities in FTIR spectra of multimineral analyses reveal information on mineral abundances [13], which can be used as a tool in mineral exploration [10].

The formula for kaolinite is $Al_2O_3 \cdot 2SiO_2 \cdot 2H_2O$, while halloysite is $Al_2O_3 \cdot 2SiO_2 \cdot 4H_2O$. When halloysite is fully hydrated, two H_2O molecules account for interlayer water, and the other two H_2O molecules are present as structurally bound OH ions [14]. The presence of OH groups in the crystal structure of kaolinite and halloysite means that these minerals are spectrally active. The presence and abundance of these phases will be recorded in FTIR spectra.

Quantification of halloysite and kaolinite based on FTIR was carried out by Janik and Keeling in the 1990s [2,15]. The authors used a partial least square on the full FTIR spectra and tested their predicted abundances against XRD and SEM quantification. They discovered that the spectral response appears to be more sensitive to low concentrations of halloysite in mixtures with kaolinite than for XRD. Moreover, quantifying the abundance of minerals in drill-core samples using spectroscopic data helps to analyse kaolin-bearing regolith rapidly [16]. However, the quantitative discrimination between halloysite and kaolinite remains problematic. Machine learning is a fast-evolving technique that was recently employed in mineral quantification based on spectral data [17–19]. These studies imply that using an ML approach on spectral and other sample characterisation techniques may result in robust prediction of kaolinite and halloysite abundance.

In this study, we used the FTIR spectra and XRD data, along with the chemistry of the samples, determined by X-ray fluorescence analysis (XRF) and the ISO-B brightness value, to predict the abundance of kaolinite and halloysite in unknown samples solely based on their FTIR spectra, chemistry, and brightness. The prediction was completed using 50 Python 3.8-based machine- and deep-learning models that were trained on the available data and eventually reduced to just one ensemble model comprising five key base regression models, used in a final voting regression model. The trained models were saved, and they can be used on new chemical and FTIR spectral data for the accurate prediction of kaolinite and halloysite abundances.

1.1. Regional and Local Geological Setting

The Noombenberry Project is located in the southwestern portion of the Archean Yilgarn Craton. The Yilgarn Craton can be subdivided into six fault-bounded terranes (Figure 1). The Noombenberry Project is situated on the margin between the South West Terrane and the Youanmi Terrane, but most of the project area falls within the South West Terrane. The South West Terrane was amalgamated onto the southwest margin of the Youanmi Terrane at ~2650 Ma; although, the exact boundary between the two terranes remains poorly defined. The South West Terrane consists of high-metamorphic-grade granitic gneisses and metasedimentary and meta-igneous rocks. Multiple phases of deformation and granite and pegmatite intrusion occurred from ~2750 to 2620 Ma [20]. The Youanmi Terrane comprises the Murchison and Southern Cross domains and consists of granites, granitic gneisses, monzogranite, clastic sedimentary units, and volcanic rocks [20,21]. The Youanmi Terrane is isotopically distinct from the other terranes in the Yilgarn Craton [20] and has an initial formation age of >3050 Ma [20,22,23].

Most of the project area is covered in a thin layer of Cenozoic sediments, including Tertiary sands and laterite and Quaternary colluvial clay, silt, and sand. According to available Geological Survey of Western Australia (GSWA) mapping, the underlying bedrock geology consists of Archean granites that can be broadly divided into pre-to-syn-tectonic granites and post-tectonic granites [24]. The Noombenberry kaolinite–halloysite deposits overlie a medium-to-coarse grained, post-tectonic, quartz monzonite. Outcrop of quartz monzonite is mapped within the tenements E77/2622, E77/2624, and E77/2724 (Figure 1, inset). Leucocratic quartz monzonite with sparse biotite is mapped within E77/5650. Pre-to-syn-tectonic granites include foliated-to-migmatitic granodiorites and tonalites. Brecciated migmatite is mapped in the southern- and northern-most tenements, E77/5649

and E77/2725, respectively. A primary iron occurrence with the Merredin-banded iron formation in E77/2622 provides evidence for the presence of greenstone belt remnants. The northwest-trending, regional-scale Koolanooka Fault that separates the South West Terrane from the Youanmi Terrane runs through tenement E77/2725 (Figure 1). Domains of amphibolite occur adjacent to this fault. Two crosscutting, east–west trending, Paleoproterozoic dolerite dykes are part of the Widgiemooltha Dolerite and appear on aeromagnetic images as prominent linear lows due to remnant magnetisation.

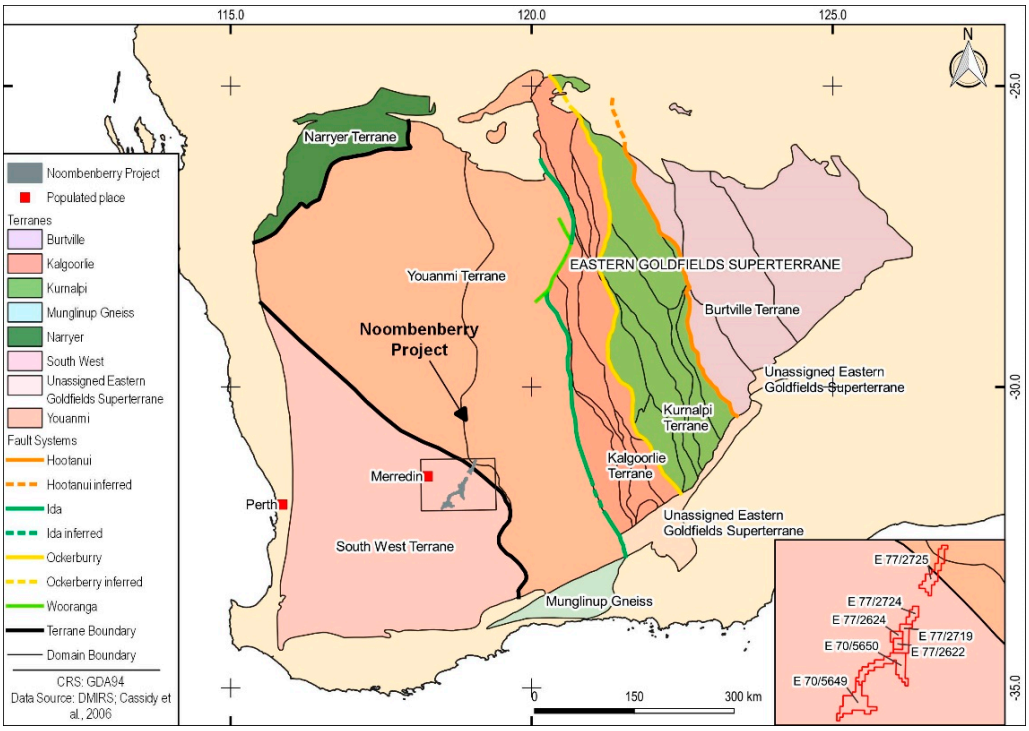

Figure 1. Terranes of the Yilgarn Craton, the Noombenberry Project in grey, predominantly lying in the South West Terrane, modified after [20].

The regolith profile at the Noombenberry Project is well developed; it grades from partially weathered granitic bedrock into saprolite, with increasing clay content towards the surface. A ~1–2 m-thick transition zone overlies the granite, transitioning from partially weathered granite to saprolitic clays (Figure 2). The pedolith and lateritic residuum sections of the weathering profile have been completely removed and are not present. Saprolite is capped directly with sandy soils and colluvium. The cover material is ~3–5 m thick and consists of reddish to yellow-brown haematitic, quartz-rich soils. The saprolite varies in thickness from <1 m overlying isolated outcropping granite to >50 m. Discontinuous pods of Fe staining occur within the saprolitic zone, which results in lower brightness values. The age of the saprolitic clay is unknown. The basement geology consists of undulating granite, which locally outcrops within the project area.

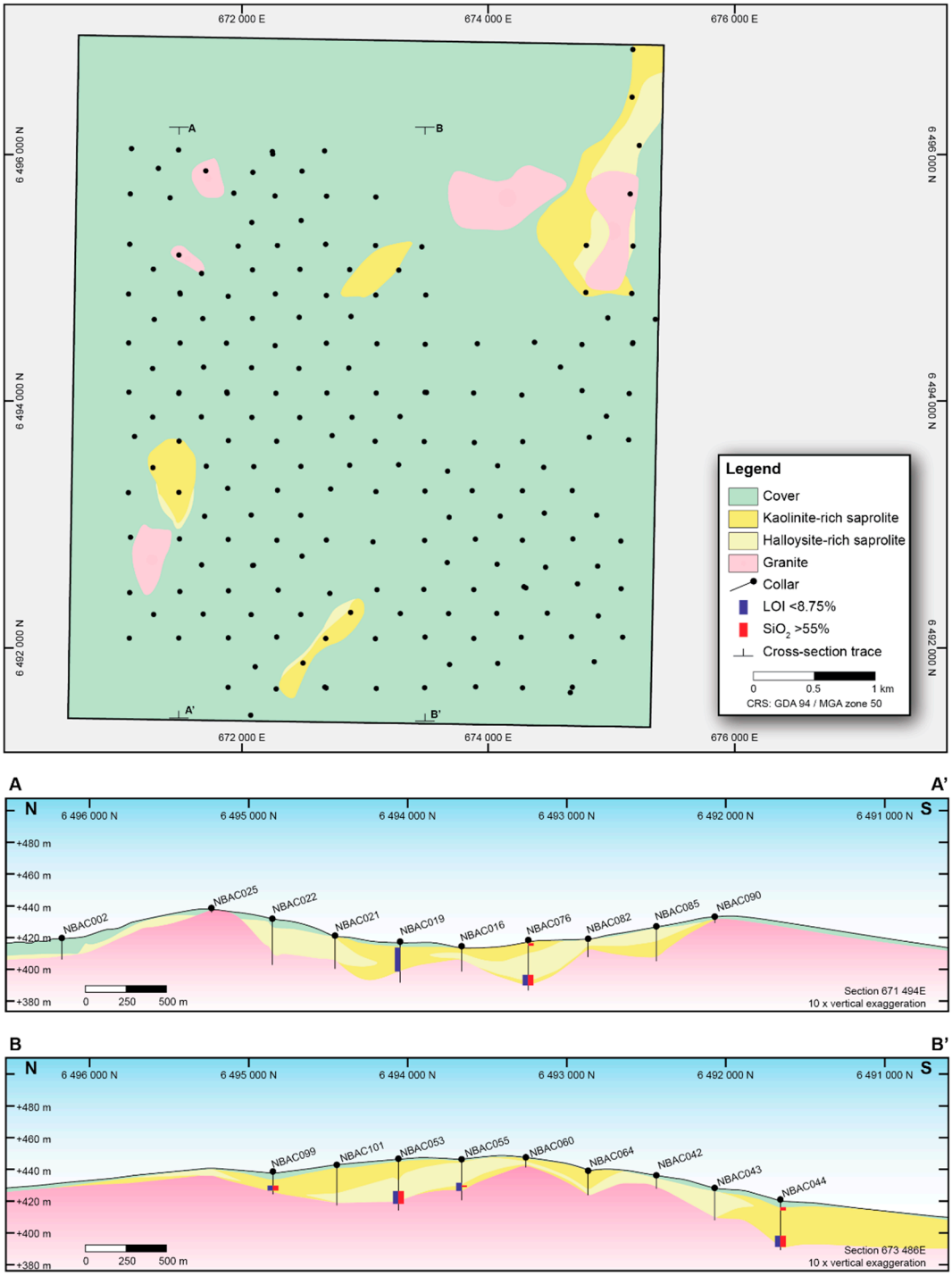

Figure 2. Overview of the surface, drill holes, and undulating fresh granite contact; (**A**) cross-section along 671 494 E (**B**) cross-section along 673 486 E.

1.2. Kaolinite and Halloysite Mineralisation

Clay deposits can be broadly grouped into residual (primary) and transported (secondary) deposits. Residual deposits form in situ through the alteration of feldspar-rich rocks (e.g., granite) by weathering or hydrothermal processes [14,25,26]. Transported deposits are produced by the movement of weathered products by water, where they are deposited in a quiescent environment some distance away from the original point of generation [27]. Residual clay deposits have not been subject to erosional transporta-

tion and redeposition processes. Mineralisation at Noombenberry is considered to be a residual deposit.

Kaolin is a white, powdery, microcrystalline material that consists of kaolinite with subordinate quartz and mica. The kaolinite group of phyllosilicate minerals includes the dioctahedral minerals kaolinite, halloysite, dickite, and nacrite. The two main clay minerals present at Noombenberry are kaolinite and halloysite. Kaolinite and halloysite are chemically and structurally similar. Kaolinite is triclinic and has a plate-like crystal habit, whereas halloysite is monoclinic and generally has a tubular morphology. Halloysite also differs from kaolinite due to the presence of interlayer water [28–31]. Halloysite contains a single layer of water molecules in each interlayer space: d_{001} varies from 7.2 Å in kaolinite to 10 Å in halloysite.

Halloysite mineralisation requires the continuous presence of water [28]. Interlayer water is extremely loosely held, and halloysite dehydration in unsaturated environments occurs at temperatures as low as room temperature and is irreversible [32]. Dehydrated halloysite is characterised by a reduced interlayer spacing (7 Å) very similar to kaolinite, making it difficult to differentiate using XRD patterns [29]. The hydrated and dehydrated halloysite end members are referred to as halloysite (10 Å) and halloysite (7 Å), respectively.

Kaolinite formation requires relatively low temperatures and pressures [26] and wet, mildly acidic conditions. This allows for the flow of K^+, Na^+, Ca^{2+}, and Mg^{2+} ions in solution and the loss of SiO_2 through leaching [33]. Locations with tropical climates, high rainfall, rapid drainage, and adequate groundwater movement to leach the soluble components are ideal for the formation of kaolinite [26]. Acidic conditions are crucial to the formation of halloysite, because the layer charge is pH dependent [33]. When pH < 8, the octahedral sheet of the halloysite layer is positively charged, while at pH > 2, the tetrahedral sheet is negatively charged. It is speculated that water molecules are retained within the interlayer space because the opposing charges of the two sheets attract different polar ends of the H_2O [33].

Kaolinite and halloysite are the major weathering products of plagioclase and K-feldspar and, to a lesser extent, muscovite and biotite, which are all present in the basement granite at Noombenberry. Feldspar may weather directly to kaolinite, or this may be preceded by halloysite [32]. Plagioclase is relatively unstable and more susceptible to weathering and will, therefore, break down before K-feldspar or muscovite [26]. The breakdown of K-feldspar to kaolinite during intense weathering occurs via the following simplified reaction:

$$2KAlSi_3O_{8(\text{K-feldspar})} + 3\ H_2O \rightarrow Al_2Si_2O_5(OH)_{4(\text{kaolinite})} + 4SiO_2 + 2K^+ \quad (1)$$

Silicon and K are leached away, and if K is not lost, illite will form instead of kaolinite [14]. Muscovite weathers to kaolinite through the intergrowth of mica and kaolinite or via an intermediate stage of montmorillonite [34]. This process requires the addition of water and protons that transform into OH groups, as well as the removal of K, via the simplified Equation:

$$2Kal_2(AlSi_3O_{10})(OH)_{2(\text{muscovite})} + 2H^+ + 3H_2O \rightarrow 1.5Al_4(Si_4O_{10})(OH)_{8(\text{kaolinite})} + 2K^+ \quad (2)$$

Kaolinite derived from muscovite can preserve the crystallographic orientation of muscovite. The transformation is likely partly topotactic (kaolinite preserves some of the octahedral sheets of muscovite), resulting in the retention of muscovite impurities (e.g., Cr and Fe) within the kaolinite [35].

Biotite also weathers to kaolinite, either directly or through an intermediate dioctahedral mica (e.g., muscovite, Reaction (3)), depending on the concentration of K^+, H^+, Al^{3+}, and Mg^{2+} ions available. Both processes are accompanied by the oxidation of Fe^{2+} to Fe^{3+} oxides or hydroxides. At high K and Al concentrations, biotite degrades in steps, from a dioctahedral Fe-rich mica, to a dioctahedral Fe-poor mica, and finally, to kaolinite (Reaction (2)), after the removal of the remaining K [35]. This takes place via the exchange

of cations (Mg^{2+}, Fe^{2+}) within octahedral layers by Al^{3+}, most likely sourced from feldspars, via the simplified equation:

$$KMg_3(AlSi_3O_{10})(OH)_{2(phlogopite)} + 2Al^{3+} \rightarrow KaI_2(AlSi_3O_{10})(OH)_{2(muscovite)} + 3Mg^{2+} \quad (3)$$

Reaction (3) could equally be written for Fe-rich biotite (annite) rather than Mg-rich biotite (phlogopite), as shown here. It is also possible for halloysite to form via biotite alteration [25].

The kaolinite and halloysite mineralisation at Noombenberry is hosted in the saprolitic and transition zone of the weathering profile, above the basement granite. The mineralisation is hosted in a lateral unit and varies from metres to tens of metres thick, depending on the depth of the undulating basal contact to fresh granite. Kaolinite is the dominant clay mineral in the saprolitic zone at the Noombenberry Project. Halloysite-rich pods or pockets contain up to 49 wt.% halloysite, and the concentration of halloysite typically decreases up the weathering profile. This is typical for halloysite mineralisation, as halloysite formation requires the constant presence of water found in the lower and wetter parts of the weathering profile [32,33]. Other minerals identified in the saprolitic zone include K-feldspar, quartz, muscovite, albite, smectite, and anatase.

Iron is a deleterious element, as it directly affects the brightness of the clay. Previous studies [36–38] indicate that the morphology of halloysite is directly linked to Fe content. Halloysite that forms long tubes typically contains a lower concentration of Fe_2O_3 compared with short-tube, spheroidal, and platy halloysite. Samples from Noombenberry examined using scanning electron microscopy (SEM) show a dominance of an elongated tubular shape, which is linked to low Fe contents in the above-cited literature.

2. Materials and Methods

2.1. Drill Samples

Two phases of drilling have been completed at the Noombenberry Project. Phase 1 drilling commenced on 11 December 2020. The holes were drilled on a 400 m × 400 m grid with an infill 200 m grid across the extent of E77/2622. A total of 197 holes were drilled at a dip of −90°, totalling 4431 m. Drilling was conducted using a truck-mounted Atlas Copco Rotamec R50 aircore drill rig.

2.2. Sample Preparation

At the drill rig, 1 m bulk samples were fed directly from the cyclone into labelled plastic bags. Selective composite sample intervals were chosen post-drilling, based on geological logging, and were collected using a PVC spear. The bulk sample bag was laid flat on the ground, and the spear was pushed from the top right corner to the bottom left corner, aiming to collect a representative sample of the full metre. Where possible, samples were collected over a nominal 4 m interval; however, shorter sample intervals were used to avoid zones of Fe staining or mixing of lithologies. No samples representing <1 m or >5 m intervals were collected.

Composite samples were not collected when a high degree of Fe-staining was identified in drill chips, as the presence of trace amounts of Fe can negatively affect the brightness of clay. Composite samples were submitted to Bureau Veritas, Adelaide, for sample preparation. Sample weights were recorded after compositing but before any subsampling or drying. Samples were dried at a low temperature (60 °C) to avoid the destruction of the halloysite. The dried sample was then pushed through a 5.6 mm screen prior to splitting. Once dry, the samples were weighed and passed through a hopper into a small rotary splitter to produce a 1 kg sample. The 1 kg splits were wet-sieved using a Kason screening deck at 180 and 45 µm. The screening deck underwent regular ultrasonic cleaning to prevent blinding. The 180–5600 µm and 45–180 µm fractions were filtered and dried on weighing papers, then photographed. All analytical work was conducted on the <45 µm fractions according to industry practice, as the sieved kaolinite represents the saleable

product. The <45 μm fraction was filtered and dried on weighing paper. Three separate splits were taken from the <45 μm fraction for XRD, XRF, and ISO-B (brightness) analysis.

2.3. X-ray Diffraction (XRD)

The mineralogical composition was analysed by XRD at CSIRO, Adelaide. A 3 g subsample was taken from the <45 μm fraction and was pulverised in a McCrone micronising mill for 10 min with ~15 mL of deionised water. The resulting slurry was placed into a 20 mL glass jar and attached to a small, compressed air-driven spray paint device. The slurry was gently agitated while spraying the contents into a cylindrical chamber heated to 150 °C, with a thermocouple-controlled belt heater to produce a spherical agglomerated sample for XRD analysis [39]. The spherical agglomerates were collected and stored in containers.

The agglomerated sample was gently poured into stainless steel sample holders. The sample holders were lightly tapped to distribute the spheres evenly, and then, any excess material was scraped off using the edge of a glass slide. Diffraction patterns were recorded using a PANalytical X'Pert Pro multi-purpose diffractometer (Malvern Panalytical Ltd, Malvern, UK) using Fe-filtered Co-Kα radiation, an automatic divergence slit, a 2° anti-scatter slit and a fast X'Celerator Si strip-detector. The diffraction patterns were recorded in steps of 0.017° 2θ with ~0.4 s counting time per step over the angle range of 4–80 2θ. Quantitative analysis was performed on the XRD data using the commercial TOtal Pattern Analysis Software package (TOPAS) from Bruker AXS (Billerica, MA, USA). The results were normalised to 100% and, therefore, do not include estimates of unidentified or amorphous material. The estimated proportions of halloysite and kaolinite were determined by profile-fitting in TOPAS. The fitting algorithm was calibrated using a suite of 20 < 2 μm fractions of samples from the Noombenberry Project analysed by XRD, SEM, and Fourier transform infrared spectroscopy (FTIR).

2.4. X-ray Fluorescence (XRF)

Whole-rock major-element analysis was conducted by XRF at Bureau Veritas, Wingfield, Adelaide, using method XRF4B. Samples were analysed for Fe_2O_3, SiO_2, Al_2O_3, CaO, K_2O, Mn, Na_2O, MgO, P, S, TiO_2, and Cl. LOI was measured by gravimetric determination. Samples were fused using a lithium borate flux and cast into a glass disc for analysis.

2.5. Fourier Transform Infrared (FTIR) Spectroscopy

Fourier transform infrared spectroscopy (FTIR) is a technique to measure how much light is absorbed and transmitted in a sample at each wavelength. To obtain an infrared (IR) spectrum (electromagnetic radiation with wavelengths longer than visible light), the raw data are converted using the mathematical process of Fourier transform into a spectrum of absorption or transmission. The FTIR analyses in this study were performed using a Thermo Scientific Nicolet iS50 FTIR Spectrometer at Bureau Veritas, Wingfield, Adelaide, Australia. For the ML approach, we used the whole spectra from the Near IR and Mid IR to the Far IR (350–44,701.59 nm over 3300 increments). A total of 839 FTIR spectra were collected.

2.6. Brightness Analysis

Brightness refers to the percentage of blue light reflected from the clay surface at a specific, effective wavelength of 457 [40]. Brightness analysis (457 nm) was carried out at the University of South Australia using a Hunterlab UltraScan PRO instrument, following the method described in the TAPPI test method T 534 om-03 [41]. Samples were prepared into 12–13 mm-deep, uniformly compacted pigment plaques, by pressing the <45 μm-size fraction into a brass cylinder. A force of 210 kPa was applied for 5 s, using a 5.73 kg weight loaded onto the ram pin.

The Hunterlab UltraScan PRO was set up to exclude reflected light (RspecEx mode) and calibrated against a standard "light trap" and a standard glossy white tile. The bright-

ness and colour measurements were captured for each sample using C/2 and D65/10 illumination sources. Each sample was placed against the measurement port of the UltraScan PRO and analysed. The data were automatically captured within the EasyMatch QC software and exported into an Excel spreadsheet. Three plaques were made for each sample, and each plaque was measured three times, totalling nine measurements per sample. The plaque was moved a small amount between each measurement, and the results of the nine analyses were averaged. Although brightness analysis is quantified as a percentage, it is industry standard to report a unitless value, i.e., a sample that reflects 80% of blue light has a brightness value of 80. Samples with high kaolinite and halloysite content and low foreign mineral content show the highest brightness values.

2.7. Machine-Learning (ML) Prediction

The assay and spectral data were merged to prepare the data for modelling. Geochemical analyses with data with missing values or missing FTIR spectra were removed from the dataset.

The kaolinite dataset consists of the following: kaolinite abundance from XRD (wt.%), Fe_2O_3 (wt.%), Al_2O_3 (wt.%), SiO_2 (wt.%), TiO_2 (wt.%), CaO (wt.%), K_2O (wt.%), Na_2O (wt.%), MgO (wt.%), P (wt.%), LOI (wt.%), brightness, and FTIR spectra from 350–44,701.59 nm over 3300 increments, for 699 samples. The kaolinite XRD, XRF, LOI, and brightness ISO-B data were log-transformed prior to modelling.

The halloysite dataset consists of the following: halloysite abundance from XRD (wt.%), predicted kaolinite (wt.%, ML algorithm output), Fe_2O_3 (wt.%), Al_2O_3 (wt.%), SiO_2 (wt.%), TiO_2 (wt.%), CaO (wt.%), K_2O (wt.%), Na_2O (wt.%), MgO (wt.%), P (wt.%), S (wt.%), LOI (wt.%), brightness, and FTIR spectra from 350 to 44,701.59 nm over 3300 increments, for 316 samples. The halloysite XRD, XRF, LOI, brightness ISO-B data, and predicted kaolinite (wt.%, ML algorithm output) data were log-transformed prior to modelling. Using the predicted kaolinite (wt.%) values in the halloysite prediction allows the relationship between kaolinite and halloysite to be incorporated into the modelling.

The objective was to model and predict the kaolinite and halloysite percentages using the geochemical analysis, spectral, and brightness data. Over 50 Python (v3.8) ML and TensorFlow/Keras deep-learning models were trained on the data and eventually reduced to just one ensemble model, comprising five key base regression models, used in a final voting regression model (Figure 3).

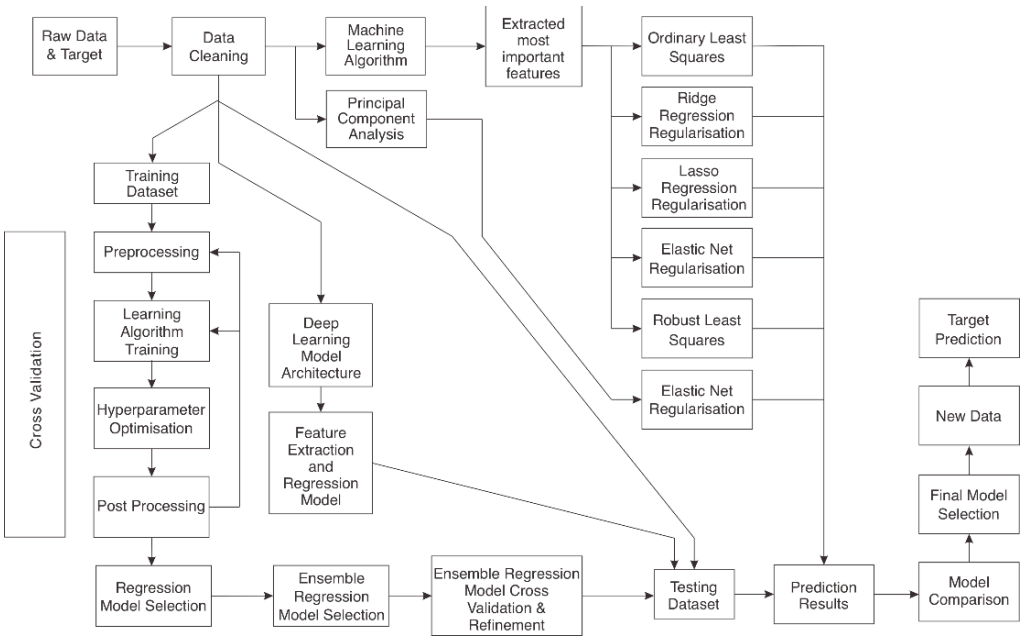

Figure 3. Schematic diagram illustrating the ML workflow.

Two other approaches were tested:

1. ML was employed to determine the most important features of the regression models. These features were then used in ordinary least square (OLS), robust least squares (RLS), and regularisation lasso, ridge, and elastic net models.
2. Principal components analysis was employed on the merged kaolinite, chemistry, and spectral dataset, and elastic net regularisation was employed to reduce the model complexity further.

3. Results

3.1. XRD Data Validation

Before predictions of kaolinite and halloysite abundance could be made, the training XRD data had to be validated to ensure that the mineral abundances were robust and reliable. This was achieved by comparing a theoretical chemical composition derived from the mineralogy (XRD data) with the measured XRF analysis for the same sample. However, kaolinite and halloysite have very similar compositions: kaolinite = $Al_2O_3 \cdot 2SiO_2 \cdot 2H_2O$ and halloysite = $Al_2O_3 \cdot 2SiO_2 \cdot 4H_2O$. So, with only a minor difference in the calculated LOI, SiO_2, and Al_2O_3 (depending on what composition is selected for halloysite) with varying halloysite: kaolinite values, it is not possible to robustly validate the halloysite and kaolinite abundances, except to conclude that the sum of halloysite and kaolinite is correct.

The minerals identified by XRD were kaolinite, halloysite, microcline, albite, oligoclase, quartz, muscovite, smectite, anatase, rutile, goethite, calcite, dolomite, zircon, and florencite. Kaolinite is the dominant mineral with a median abundance of 80 wt.% (maximum of 99 wt.%). Halloysite ranges up to 49 wt.%; however, in some samples, it is below the detection limit. Microcline, quartz, and muscovite occur at a median of 7.0, 2.2 and 2.1 wt.%, respectively. The remaining minerals typically occur as minor or trace components. The minerals were quantified using the Rietveld method, resulting in the weight percentages of each mineral phase normalised to 100% for each sample (e.g., 81.7 wt.% kaolinite, 9 wt.% quartz, 3.4 wt.% anatase, 2.6 wt.% halloysite, 2.6 wt.% muscovite, and 1 wt.% microcline for sample 1000795). Since the chemical composition, including volatile content (H_2O, CO_2), of each mineral composition can be inferred, the mineral abundances allow for calculation of the chemical bulk composition of the individual sample. For this calculation, the mineral compositions were obtained from published generic mineral compositions based on electron-probe microanalysis [14]. The main components, SiO_2, Al_2O_3, K_2O, Na_2O, Fe_2O_3, and the LOI, were calculated from the XRD data. The median total was 99.84 wt.% for the 839 analyses. Ten samples were not considered for the calculation because they contained amorphous material, which does not reveal structural or compositional information in XRD. Minerals that were reported to occur in the XRD data but were assigned to the abundance of <1 wt.% have been substituted to 0.5 wt.% in the calculations. This approach allowed for the addition of trace minerals to the chemical calculations, which led to a robust representation of the mineralogical suite.

The bulk composition, calculated from XRD data, was compared with the chemical composition directly obtained from XRF analyses to provide an independent check on the mineral abundance quantifications by XRD. The comparison between the two bulk compositions is presented in Figure 4. The Pearson correlation coefficient (PCC, −1 = ideal negative correlation, 0 = no correlation, 1 = ideal positive correlation) is 0.99 for K_2O, 0.98 for Na_2O, 0.93 for SiO_2, 0.92 for Al_2O_3, 0.68 for Fe_2O_3, and 0.98 for LOI. The major rock-forming components present in the key minerals at the Cloud Nine deposit (namely SiO_2, Al_2O_3, K_2O, Na_2O, and LOI) have very good correlations between the bulk composition calculated from XRD data compared with the chemical composition from XRF, with PCC values >0.92. This suggests that the quantification of the mineralogy by XRD is robust. Moreover, the data points plot along the 1:1 line in Figure 4 indicate a very good fit.

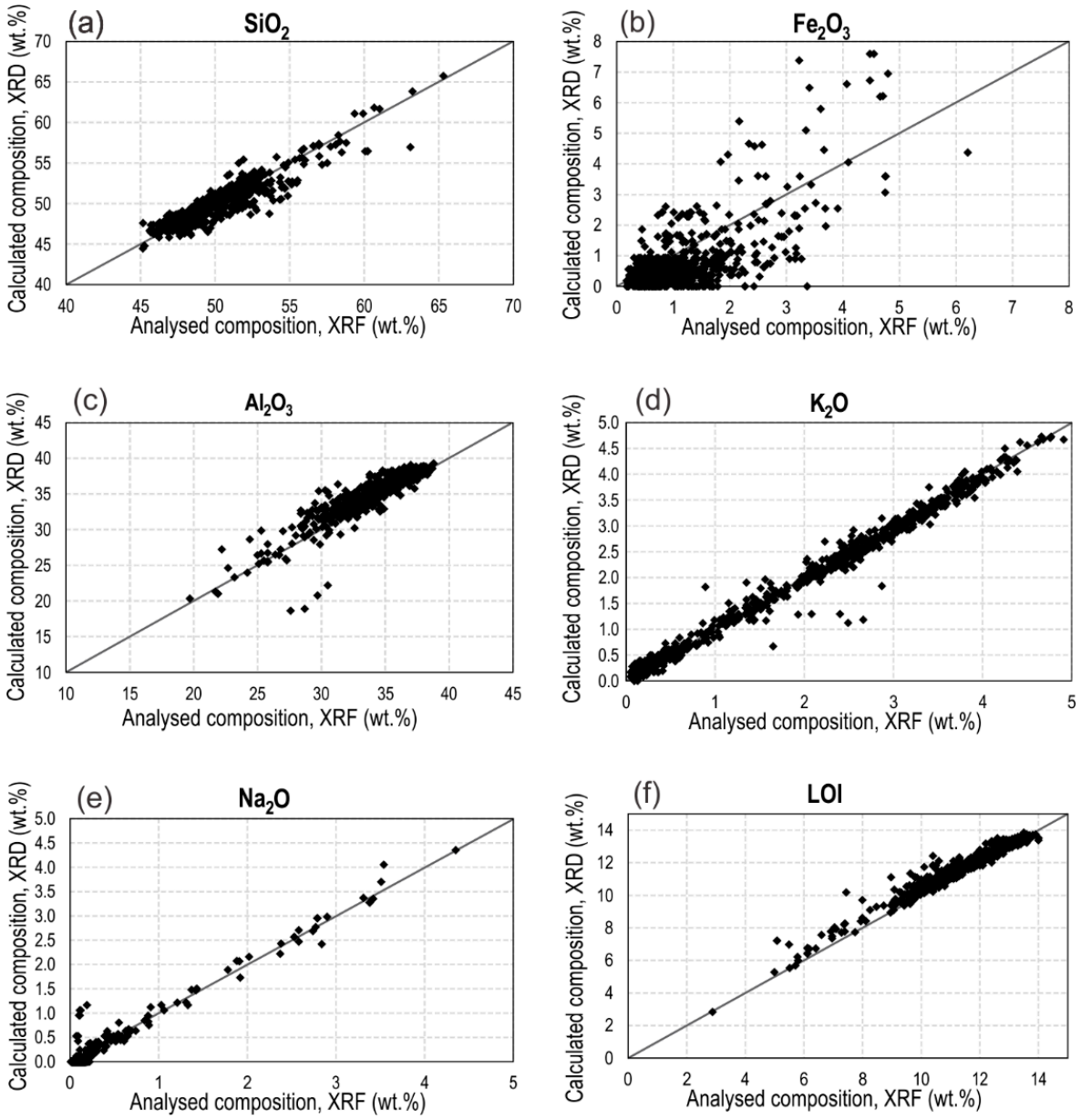

Figure 4. Bulk composition plots for XRF value vs. calculated bulk composition from XRD data for the main components: (**a**) SiO_2; (**b**) Fe_2O_3; (**c**) Al_2O_3; (**d**) K_2O; (**e**) Na_2O; (**f**) LOI ($H_2O + CO_2$). The one-to-one line is shown.

The XRF data can be compared with individual minerals among the whole dataset. Iron has a positive correlation (PCC $\geq$ 0.4) with goethite, smectite, and muscovite, suggesting that samples rich in these minerals have higher Fe concentrations. However, Fe has the poorest correlation between XRD and XRF data in Figure 4, which may indicate a heterogeneous composition of the sheet silicates, smectite and muscovite, depending on sample location. Apart from the Fe-oxide goethite, smectite is the main source of Fe (PCC = 0.73). For example, sample 1000362 (hole NBAC047, 17–18 m interval) comprises anomalous Fe_2O_3 (4.5 wt.%) and contains 20 wt.% smectite, while goethite was not detected by XRD.

3.2. Mineral and Chemical Relationships

Since halloysite and kaolinite are formed from the weathering of granite, it is important to identify samples that are not completely weathered or have been affected by other processes. After completing exploratory data analysis, considering chemical, mineralogical,

and spatial parameters, it was apparent that samples with low LOI are typically adjacent to the lower contact with the granite (Figure 2) and represent incompletely weathered granite. Therefore, an LOI cut-off of <8.75% was selected based on the probability plot (Figure 5a). The samples with LOI <8.75% typically contained greater amounts of SiO_2 (Figure 5b) and the least kaolinite (Figure 5c). This is consistent with the breakdown of K-feldspar to kaolinite during intense weathering occurring via reaction 1, which produces $4SiO_2$ and $2K^+$. If SiO_2 was not leached away, it would follow that these samples were enriched in that element, and that if SiO_2 was not leached away, then K may not have been either; these samples may be higher in muscovite and illite (Figure 5d). Most of the samples that are highest in SiO_2 are located near the lower contact with the granite (Figure 2); however, some are found higher up the weathering profile. Some SiO_2-rich units are midway up the profile, which may represent small silcrete units, and some are at or near the surface, which may represent sands.

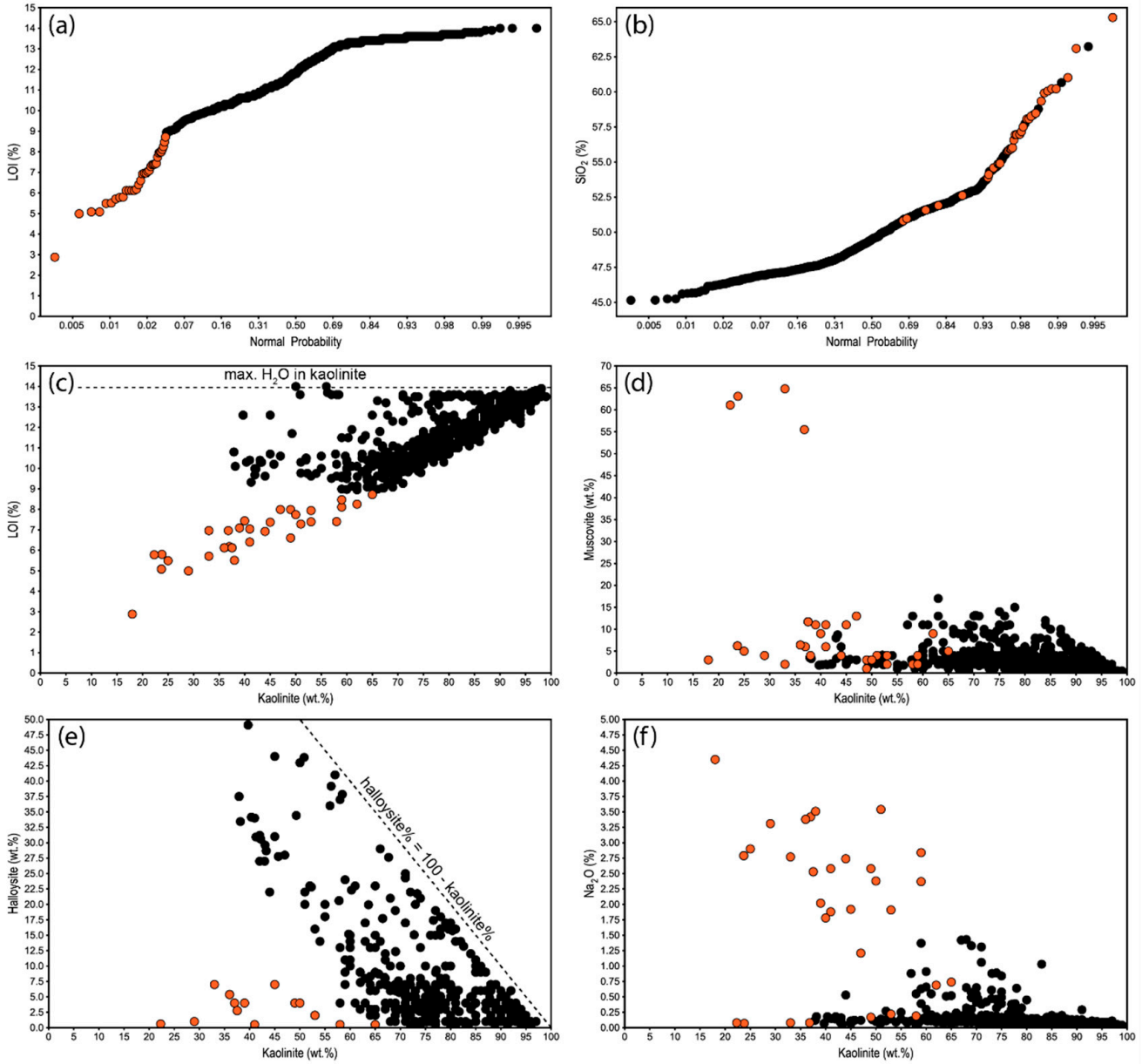

Figure 5. (**a**) Normal probability plot for LOI (<8.75% coloured orange in this and following panels); (**b**) normal probability plot for SiO_2; (**c**) kaolinite (wt.%) vs. LOI (wt.%); (**d**) kaolinite (wt.%) vs. muscovite (wt.%); (**e**) kaolinite (wt.%) vs. halloysite (wt.%); (**f**) kaolinite (wt.%) vs. Na_2O (wt.%).

Halloysite and kaolinite have a strong negative relationship (Figure 5e), and they dominate many of the samples, with only a small additional component of ~2% SiO_2 present in the most clay-rich samples. The samples with LOI <8.75% do not fall on the trend and are anomalously low in LOI compared with the rest of the population. Finally, the samples with low LOI typically have higher Na contents (Figure 5f), which corresponds to high albite in these samples. The presence of albite in these samples is consistent with trends in the regional magnetic data of magnetic ridges (structures), being associated with the areas of highest halloysite concentration. Around these structures, there may be some hydrothermal alteration (including albite) of the granite.

Samples with an LOI <8.75% were excluded from ML prediction, as they do not represent fully weathered granite and, thus, should not be included in that domain (Figure 5a,c).

3.3. FTIR Spectra

Spectra recorded by FTIR provide information on the chemical composition and features of the mineralogical samples. Some of the FTIR spectra have been investigated in detail to discriminate halloysite from kaolinite and compare the spectra with the USGS spectral library and literature [42]. Halloysite-rich samples have greater H_2O intensities in the 1900 nm range relative to pure kaolinite samples (Figure 6a), which is expected due to the interlayer water component in halloysite [43]. This effect is even more pronounced in the reference spectra showing pure mineral concentrates (Figure 6b). Absorption features for the H_2O intensity in the analysed samples in this study are consistently shifted to lower wavelengths for halloysite-rich samples (~1912 nm) relative to pure kaolinite-rich samples (~1915 nm; Table 1). Moreover, the absorption features and shapes of the OH-stretching bands differ between pure kaolinite and kaolinite–halloysite mixtures. In the latter, the OH-doublet absorption feature is ~70% further apart compared with pure kaolinite (see inset in Figure 6a). The absorption feature for the second OH-intensity is also consistently shifted by 1 nm (Table 1). The absorption feature shapes of the intensities at ~2700 nm are also susceptible to the halloysite/kaolinite ratio (cf. Figure 6a,b), with narrower features encountered for halloysite-rich samples. The described differences within the 500–3000 nm spectral range observed in Figure 6 are picked up in detail by the machine-learnt model. For the machine-learnt model, the spectral range of 350–44,701.59 nm was considered.

3.4. Kaolinite Machine-Learnt Model

Multiple models were assessed to identify the best approach to predict kaolinite (wt.%) from Fe_2O_3 (wt.%), Al_2O_3 (wt.%), SiO_2 (wt.%), TiO_2 (wt.%), CaO (wt.%), K_2O (wt.%), Na_2O (wt.%), MgO (wt.%), P (wt.%), LOI (wt.%), brightness, and FTIR spectra from 350–44,701.59 nm. To assess the model performance, the mean absolute error (MAE) was used along with the R^2. The MAE is a measure of how big an error can be expected from the forecast on average and is robust to data with outliers. In ML, negative MAE is used for optimisation, with a value of 0 representing no errors. Models are ranked from best to worst in the table below (Table 2). The ML ensemble model provided the best prediction performance. In contrast, the other six models (RLS, EN, Lasso, RR, OLS, and EN PCA 5) produced simpler, easily explainable models, but with lower accuracy (Table 2). The high dimensional data used for modelling here, in which the number of features (p) is much larger than the number of observations (n), is handled much better by the ML algorithms, which can analyse high dimensional non-linear systems much better than the rest of the modelling methods. The ML ensemble model evaluation was completed by shuffled K-fold model cross-validation (K number of splits = 10, repeats = 3) of the test data (20% of the full dataset). Boxplots of these results are presented in Figure 7.

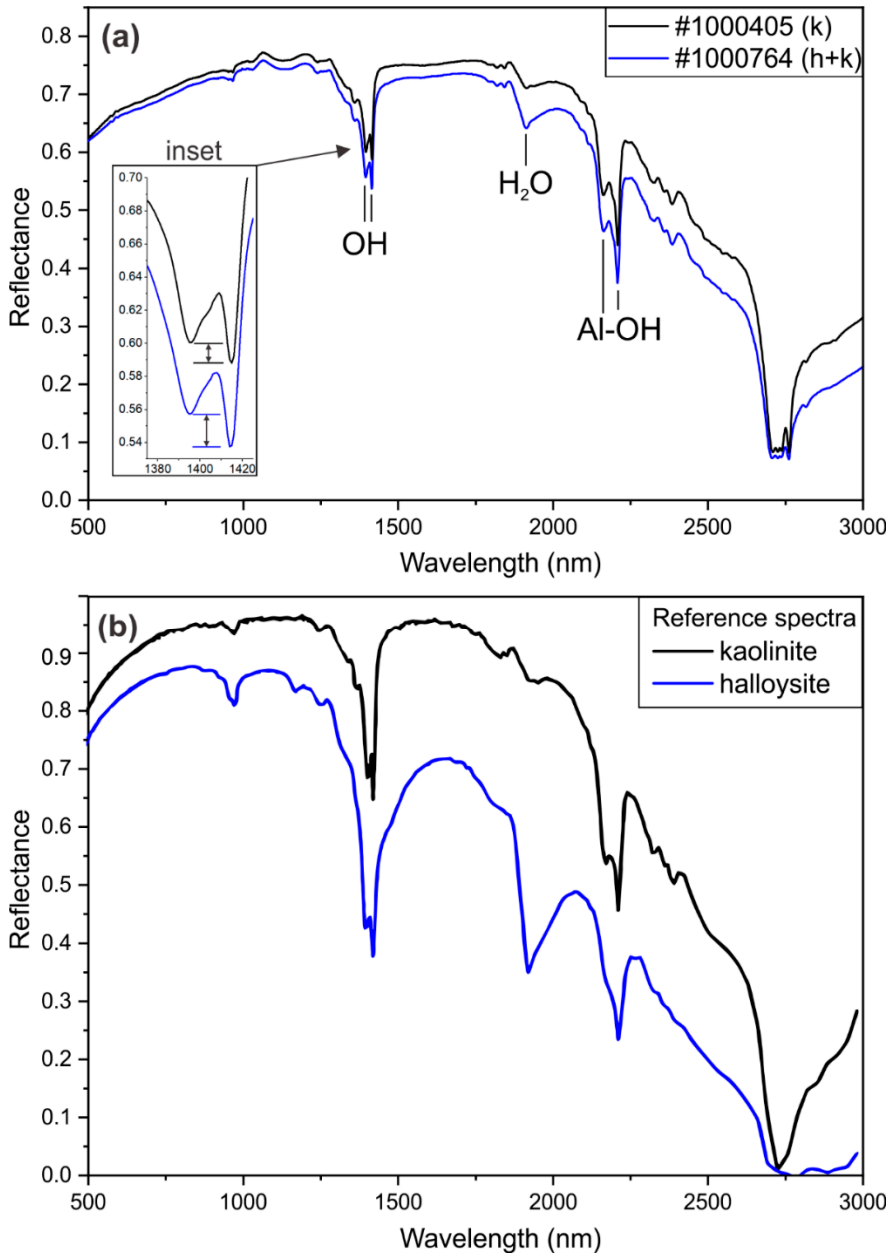

Figure 6. (**a**) Extracts of representative FTIR spectra from the project for samples 1000405 (98 wt.% kaolinite) and 1000764 (51 wt.% kaolinite, 44 wt.% halloysite). Note the differences in the H_2O intensities and OH-doublets. The inset illustrates the OH stretching band intensity ratio (c.f. [31]); (**b**) reference spectra from the USGS spectral library [42], for kaolinite (splib07a rec = 6043) and halloysite (splib07a rec = 4695).

Table 1. List of the absorption feature positions of assigned bands of pure kaolinite samples (k) and mixtures of kaolinite and halloysite with up to 44 wt.% halloysite (k + h).

Sample	Mineralogy	OH-Doublet (nm)		H_2O (nm)	Al-OH-Doublet (nm)	
1000681	k	1395	1415	1915	2163	2208
1000405	k	1395	1415	1914	2163	2208
1000679	k	1395	1415	1915	2162	2208
1000601	k + h	1395	1414	1913	2163	2208
1000735	k + h	1395	1414	1912	2163	2208
1000764	k + h	1395	1414	1912	2162	2208

Table 2. Results of the kaolinite models.

Model	R^2	MAE	Description of Models
ML ensemble	0.97	−0.052	Ensemble ML: create multiple models and then combine them to produce improved results.
RLS	0.85	−0.076	ML to derive most important features followed by robust least squares
EN	0.65	−0.081	ML to derive most important features followed by elastic net regularisation
Lasso	0.65	−0.082	ML to derive most important features followed by lasso regression regularisation
RR	0.64	−0.082	ML to derive most important features followed by ridge regression regularisation
OLS	0.65	−0.082	ML to derive most important features followed by ordinary least squares
EN PCA 5	0.47	−0.104	Principal component analysis on all features followed by elastic net regularisation

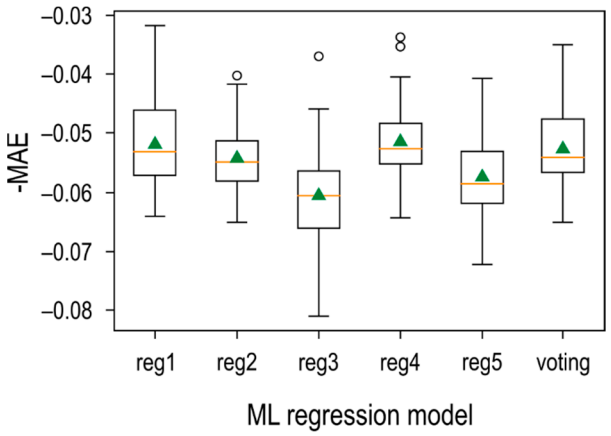

Figure 7. Boxplots of kaolinite ML model evaluation.

Ensemble methods are techniques that create multiple models and then combine them to produce improved results. Ensemble methods usually produce more accurate solutions than a single model would. For the final voting algorithm (Figure 7), weighted averaging of the base models is used. Weighted averaging is a slightly modified version of simple averaging, where the prediction of each base model is multiplied by the weight, and then, the average is calculated for the voting model. This method often reduces overfit and creates a smoother regression model. On this basis, the ML ensemble is the preferred approach to predict the kaolinite abundance.

The comparison of the kaolinite (wt.%) measured by XRD and predicted kaolinite (wt.%) by the ML ensemble is presented in Figure 8; it has an excellent R^2 = 0.97 and an MAE of −0.052. The R^2 and MAE of all the models tested are summarised in (Table 2). It is important to note that the R^2 of 0.97 was only achieved by combining all techniques in the ML ensemble (FTIR, XRF, LOI, and brightness data). When solely employing FTIR data, the R^2 is 0.93, suggesting that FTIR is the key technique to predict the mineral abundance. However, without the input of XRF, LOI, and brightness data, the prediction is not as robust.

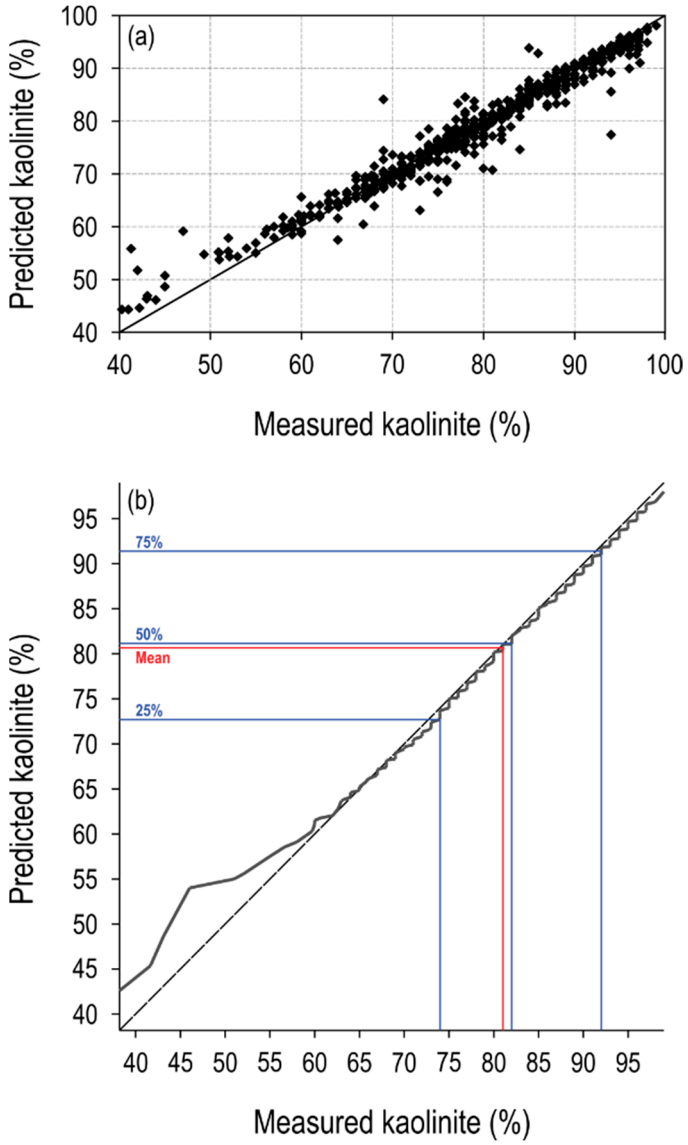

Figure 8. Kaolinite ML results (n = 699 samples); (**a**) measured kaolinite (XRD) vs. predicted kaolinite (ML) in weight percent; (**b**) as for (**a**) but for QQ plot.

3.5. Halloysite Machine-Learnt Model

The halloysite ML ensemble model uses the output from the kaolinite ML ensemble model above (along with XRF data, LOI, brightness, and FTIR spectra—analogous to 3.4) to predict the halloysite percentages. The training data for halloysite were set at halloysite >5 wt.%, where the quantification of halloysite by XRD should be reliable. The model has an excellent R^2 = 0.96 (Figure 9) and an MAE = −0.6 (Figure 10). Boxplot results of repeated shuffled K-fold model cross-validation (K number of splits = 10, repeats = 3) of test data (20% of the full dataset) are presented in Figure 10. Based on the significantly improved performance of the ML ensemble approach to model kaolinite, only this approach was used to predict halloysite abundance.

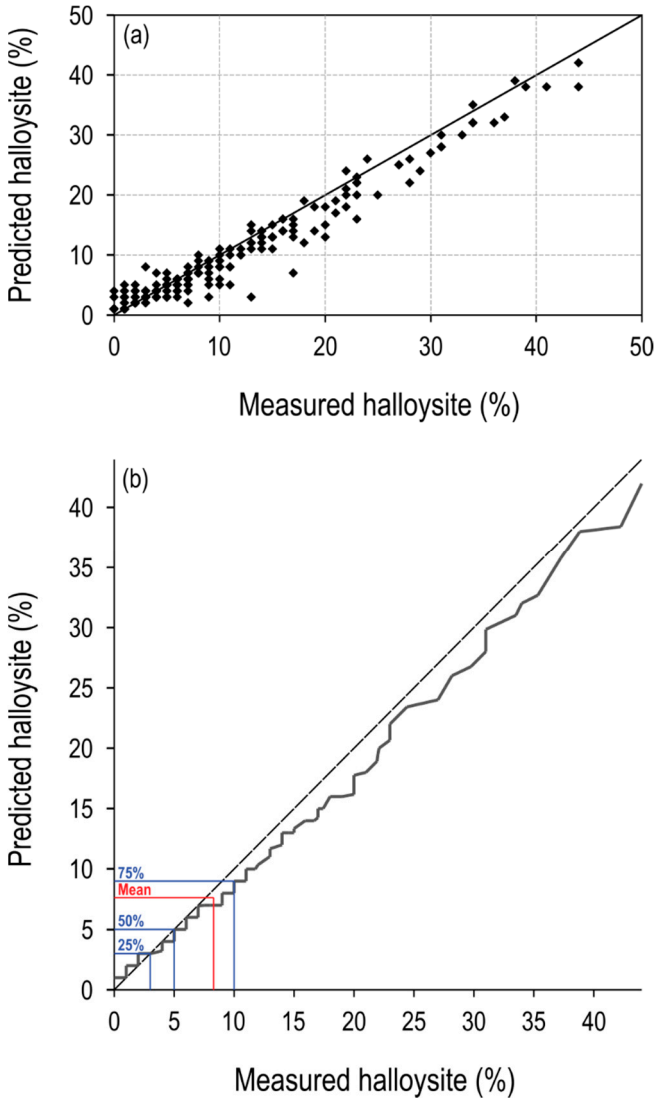

Figure 9. Halloysite ML results (n = 316 samples); (**a**) measured halloysite (XRD) vs. predicted halloysite (ML); (**b**) as for (**a**) but for QQ plot; red = mean.

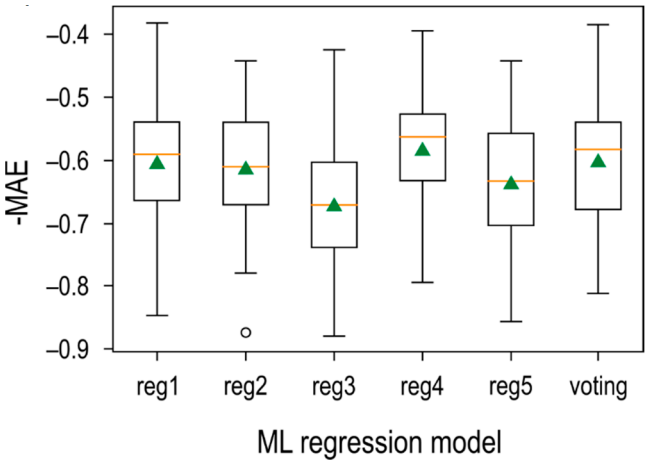

Figure 10. Boxplots of halloysite ML model evaluation.

4. Discussion and Implications

The goal of this study was to improve the quantification of kaolinite and halloysite (the two main clay minerals present at Noombenberry) by using ML and FTIR, chemical, and brightness data. The FTIR technique requires minimal sample preparation and is more cost and time effective than XRD. To accurately differentiate halloysite from kaolinite by XRD requires chemical and physical treatment prior to the XRD analyses; small quantities of halloysite are further challenging to detect in kaolinite-rich samples due to overlapping peaks in XRD patterns [2]. Conversely, FTIR requires minimal sample preparation and is considered more cost and time effective than XRD; the individual intensities in FTIR spectra of multimineral analyses can contain information on mineral abundances [10,13].

Previous studies have demonstrated the effectiveness of FTIR to quantify kaolinite and halloysite and have highlighted the benefits of FTIR over XRD when concentrations of kaolinite and halloysite in samples are low [2,13,15]. Researchers recently started implementing ML on mineral quantification based on spectral data [11,17–19]. For example, hyperspectral data collected on drill core samples paired with hierarchical density-based clustering algorithms were reported to assist in the rapid identification of differing lithologies, alteration, and/or weathering overprints [12]. However, to our knowledge, ML has not been previously used to predict halloysite and kaolinite abundance in clay samples.

Combining the FTIR technique with brightness analyses and XRF data and implementing ML algorithms resulted in an exceptional prediction of kaolinite (R^2 = 0.97 and an MAE of −0.052) and halloysite (R^2 = 0.96 and an MAE = −0.6) when compared with XRD quantification. The trained models for both kaolinite (wt.%) and halloysite (wt.%) have been saved and can be used on new chemical and FTIR spectral data for the prediction of kaolinite and halloysite abundance. Exploratory data analysis of the dataset from the project considered chemical, mineralogical, and spatial parameters and demonstrated that samples that have low LOI are typically adjacent to the lower contact with the granite and represent incompletely weathered granite. A cut-off of LOI < 8.75% was selected based on the probability plot, and samples with an LOI < 8.75% were excluded from ML prediction; these samples (4.2% of the dataset) were excluded from further analyses.

The comparisons between the ML ensemble model prediction and the XRD data for kaolinite and halloysite clearly illustrate the effectiveness of combining the XRD, brightness, and FTIR data with ML algorithms. If the FTIR approach is to be used to quantify kaolinite and halloysite abundance in new samples, a subset (e.g., 5%) of these samples should be sent for XRD analysis to provide additional training data as new parts of the deposit are drilled, and/or to provide an independent (umpire) check on the predicted kaolinite and halloysite values.

The QQ plots (Figures 8 and 9) reveal a bias with low kaolinite abundances having higher predicted abundances than measured (average bias of ~10% below 60 wt.%); correspondingly, high predicted halloysite abundances are slightly higher than measured halloysite abundances. Most of the samples examined in this dataset (85%) have kaolinite abundances >65 wt.% and <7% halloysite. At these abundances, the ML prediction is robust, as highlighted by the excellent R^2 values for the comparison between predicted and measured values. The lack of high halloysite samples that would enable the prediction to be robust at these abundances could be addressed through additional targeted sampling; to add more high-halloysite, low-kaolinite samples to the population, the models can then be regenerated. This approach is preferable to any synthetic up-sampling or down-sampling approach to deal with the distribution of the population used to train models. Any modelling approach will always be limited by the data available, and the present case is no different.

The methodology described in this paper provides a cost-effective alternative to traditional methodologies to quantify kaolinite and halloysite abundances. It may be possible to directly use the models developed here at other kaolinite–halloysite projects. However, new training data should be collected, and new models generated.

Author Contributions: Conceptualisation, M.F.G.; methodology, M.F.G. and P.I.D.P.; software, P.I.D.P.; validation, P.I.D.P., M.F.G. and M.K.; resources, T.B. and L.F.F.; data curation, S.L.T.; writing—original draft preparation, S.L.T., E.F.T., P.I.D.P. and M.F.G.; writing—review and editing, M.K., T.B. and L.F.F.; visualisation, T.B. All authors have read and agreed to the published version of the manuscript.

Funding: This research was funded by Latin Resources Limited.

Data Availability Statement: Not applicable.

Acknowledgments: The authors are grateful for the support of Latin Resources Limited, in particular Tony Greenaway, and Ross Cameron for logistical support, data, and for permission to publish this work. The authors acknowledge the comments of Mark Simpson, two journal reviewers, and the very insightful comments of the editor.

Conflicts of Interest: The authors declare no conflict of interest.

References

1. Theng, B.; Churchman, G.; Whitton, J.; Claridge, G. Comparison of intercalation methods for differentiating halloysite from kaolinite. *Clays Clay Miner.* **1984**, *32*, 249–258.
2. Janik, L.J.; Keeling, J.L. *Quantitative Determination of Halloysite Using Ft-Ir Pls Analysis and Its Application to the Characteri-Sation of Kaolins from North-Western Eyre Peninsula, South Australia*; Division of Soils Divisional Report; CSIRO Publishing: Canberra, Australia, 1996; p. 129.
3. Linker, R.; Shmulevich, I.; Kenny, A.; Shaviv, A. Soil identification and chemometrics for direct determination of nitrate in soils using FTIR-ATR mid-infrared spectroscopy. *Chemosphere* **2005**, *61*, 652–658. [CrossRef] [PubMed]
4. Terra, F.S.; Demattê, J.A.; Rossel, R.V. Spectral libraries for quantitative analyses of tropical Brazilian soils: Comparing vis–NIR and mid-IR reflectance data. *Geoderma* **2015**, *255–256*, 81–93. [CrossRef]
5. Recena, R.; Fernández-Cabanás, V.M.; Delgado, A. Soil fertility assessment by Vis-NIR spectroscopy: Predicting soil functioning rather than availability indices. *Geoderma* **2019**, *337*, 368–374. [CrossRef]
6. Xu, X.; Du, C.; Ma, F.; Shen, Y.; Wu, K.; Liang, D.; Zhou, J. Detection of soil organic matter from laser-induced breakdown spectroscopy (LIBS) and mid-infrared spectroscopy (FTIR-ATR) coupled with multivariate techniques. *Geoderma* **2019**, *355*, 113905. [CrossRef]
7. Goydaragh, M.G.; Taghizadeh-Mehrjardi, R.; Golchin, A.; Jafarzadeh, A.A.; Lado, M. Predicting weathering indices in soils using FTIR spectra and random forest models. *CATENA* **2021**, *204*, 105437. [CrossRef]
8. Goydaragh, M.G.; Taghizadeh-Mehrjardi, R.; Jafarzadeh, A.A.; Triantafilis, J.; Lado, M. Using environmental variables and Fourier Transform Infrared Spectroscopy to predict soil organic carbon. *CATENA* **2021**, *202*, 105280. [CrossRef]
9. Barra, I.; Haefele, S.M.; Sakrabani, R.; Kebede, F. Soil Spectroscopy with the Use of Chemometrics, MACHINE learning and Pre-processing Techniques in Soil Diagnosis: Recent advances—A review. *Trends Anal. Chem.* **2020**, *135*, 116166. [CrossRef]
10. Laukamp, C.; Rodger, A.; LeGras, M.; Lampinen, H.; Lau, I.; Pejcic, B.; Stromberg, J.; Francis, N.; Ramanaidou, E. Mineral Physicochemistry Underlying Feature-Based Extraction of Mineral Abundance and Composition from Shortwave, Mid and Thermal Infrared Reflectance Spectra. *Minerals* **2021**, *11*, 347. [CrossRef]
11. Desta, F.; Buxton, M.; Jansen, J. Data Fusion for the Prediction of Elemental Concentrations in Polymetallic Sulphide Ore Using Mid-Wave Infrared and Long-Wave Infrared Reflectance Data. *Minerals* **2020**, *10*, 235. [CrossRef]
12. Rodger, A.; Fabris, A.; Laukamp, C. Feature Extraction and Clustering of Hyperspectral Drill Core Measurements to Assess Potential Lithological and Alteration Boundaries. *Minerals* **2021**, *11*, 136. [CrossRef]
13. Kaufhold, S.; Hein, M.; Dohrmann, R.; Ufer, K. Quantification of the mineralogical composition of clays using FTIR spectroscopy. *Vib. Spectrosc.* **2012**, *59*, 29–39. [CrossRef]
14. Deer, W.; Howie, R.; Zussman, J. *An Introduction to the Rock-Forming Minerals*, 2nd ed.; Longman Scientific and Technical: Harlow, UK, 1992; p. 696.
15. Janik, L.J.; Keeling, J. FT-IR Partial Least-Squares Analysis of Tubular Halloysite in Kaolin Samples from the Mount Hope Kaolin Deposit. *Clay Miner.* **1993**, *28*, 365–378. [CrossRef]
16. Haest, M.; Cudahy, T.; Laukamp, C.; Gregory, S. Quantitative Mineralogy from Infrared Spectroscopic Data. II. Three-Dimensional Mineralogical Characterization of the Rocklea Channel Iron Deposit, Western Australia. *Econ. Geol.* **2012**, *107*, 229–249. [CrossRef]
17. Barker, R.D.; Barker, S.L.; Cracknell, M.J.; Stock, E.D.; Holmes, G. Quantitative Mineral Mapping of Drill Core Surfaces II: Long-Wave Infrared Mineral Characterization Using μXRF and Machine Learning. *Econ. Geol.* **2021**, *116*, 821–836. [CrossRef]
18. Chen, T.; Zhang, T.; Li, H. Applications of laser-induced breakdown spectroscopy (LIBS) combined with machine learning in geochemical and environmental resources exploration. *TrAC Trends Anal. Chem.* **2020**, *133*, 116113. [CrossRef]
19. De La Rosa, R.; Khodadadzadeh, M.; Tusa, L.; Kirsch, M.; Gisbert, G.; Tornos, F.; Tolosana-Delgado, R.; Gloaguen, R. Mineral quantification at deposit scale using drill-core hyperspectral data: A case study in the Iberian Pyrite Belt. *Ore Geol. Rev.* **2021**, *139*, 104514. [CrossRef]

20. Cassidy, K.; Champion, D.; Krapez, B.; Barley, M.; Brown, S.; Blewett, R.; Groenewald, P.B.; Tyler, I.M. *A Revised Geological Framework for the Yilgarn Craton, Western Australia*; Record 2006/8; Geological Survey of Western Australia: East Perth, Australia, 2006.
21. Cassidy, K.F.; Champion, D.C.; McNaughton, N.; Fletcher, I.; Whitaker, A.J.; Bastrakova, I.V.; Budd, A. *Characterisation and Metallogenic Significance of Archaean Granitoids of the Yilgarn Craton, Western Australia: Results of Research Carried Out as MERIWA Project No. M281 at the Key Centre for Strategic Mineral Deposits, the University of Western Australia and Australian Geological Survey Organisation*; Minerals and Energy Research Institute of Western Australia: East Perth, Australia, 2002.
22. Barley, M.E.; Brown, S.J.A.; Cassidy, K.; Champion, S.J.; Krapez, B. *An Integrated Geological and Metallogenic Framework for the Eastern Yilgarn Craton: Developing Geodynamic Models of Highly Mineralised Archaean Granite-Greenstone Terranes*; AMIRA Project; Australian Minerals Industry Research Association: East Perth, Australia, 2003; p. 624.
23. Griffin, W.; Belousova, E.; Shee, S.; Pearson, N.; O'Reilly, S.Y. Archean crustal evolution in the northern Yilgarn Craton: U–Pb and Hf-isotope evidence from detrital zircons. *Precambrian Res.* **2004**, *131*, 231–282. [CrossRef]
24. Jones, P.; Trendall, A. *Southern Cross 1:250 000 Geological Series Map, Sheet SH 50-16*; Geological Survey of Western Australia: East Perth, Australia, 1981.
25. Kretzschmar, R.; Robarge, W.; Amoozegar, A.; Vepraskas, M. Biotite alteration to halloysite and kaolinite in soil-saprolite profiles developed from mica schist and granite gneiss. *Geoderma* **1997**, *75*, 155–170. [CrossRef]
26. Murray, H.H. Kaolin minerals: Their genesis and occurrences; Chapter 4. In *Hydrous Phyllosilicates*; De Gruyter: Boston, MA, USA, 1988; pp. 67–90. [CrossRef]
27. Abeysinghe, P.; Fetherston, J.M. *Kaolin in Western Australia*; Geological Survey of Western Australia: East Perth, Australia, 1999.
28. Churchman, G.; Carr, R. The definition and nomenclature of halloysites. *Clays Clay Miner.* **1975**, *23*, 382–388. [CrossRef]
29. Hillier, S.; Ryan, P. Identification of halloysite (7 Å) by ethylene glycol solvation: The 'MacEwan effect'. *Clay Miner.* **2002**, *37*, 487–496. [CrossRef]
30. Drits, V.A.; Sakharov, B.A.; Hillier, S. Phase and structural features of tubular halloysite (7 Å). *Clay Miner.* **2018**, *53*, 691–720. [CrossRef]
31. Hillier, S.; Drummond-Brydson, R.; Delbos, E.; Fraser, T.; Gray, N.; Pendlowski, H.; Phillips, I.; Robertson, J.; Wilson, I. Correlations among the mineralogical and physical properties of halloysite nanotubes (HNTs). *Clay Miner.* **2016**, *51*, 325–350. [CrossRef]
32. Yuan, J. Clay Mineralogy and Its Influence on Industrial Uses of Some Kaolin Clay Deposits from South China and Eastern Washington-Idaho, United States of America. Ph.D. Thesis, Indiana University, Bloomington, IN, USA, 1994.
33. Churchman, G.J.; Pasbakhsh, P.; Lowe, D.; Theng, B. Unique but diverse: Some observations on the formation, structure and morphology of halloysite. *Clay Miner.* **2016**, *51*, 395–416. [CrossRef]
34. Stoch, L.; Sikora, W. Transformations of micas in the process of kaolinitization of granites and gneisses. *Clays Clay Miner.* **1976**, *24*, 156–162. [CrossRef]
35. Singh, B.; Gilkes, R. Weathering of a chromian muscovite to kaolinite. *Clays Clay Miner.* **1991**, *39*, 571–579. [CrossRef]
36. Nagasawa, K.; Noro, H. Mineralogical properties of halloysites of weathering origin. *Chem. Geol.* **1987**, *60*, 145–149. [CrossRef]
37. Noro, H. Hexagonal platy halloysite in an altered tuff bed, Komaki City, Aichi Prefecture, Central Japan. *Clay Miner.* **1986**, *21*, 401–415. [CrossRef]
38. Wada, S.-I.; Mizota, C. Iron-rich halloysite (10A) with crumpled lamellar morphology from Hokkaido, Japan. *Clays Clay Miner.* **1982**, *30*, 315–317. [CrossRef]
39. Hillier, S. Use of an air brush to spray dry samples for X-ray powder diffraction. *Clay Miner.* **1999**, *34*, 127–135. [CrossRef]
40. South African Pulp and Paper Industries. Understanding Paper Brightness. 2017. Available online: https://cdn-s3.sappi.com/s3fs-public/sappietc/Understanding%20Paper%20Brightness.pdf (accessed on 18 August 2021).
41. Technical Association of the Pulp and Paper Industry. *Brightness of Clay and Other Mineral Pigments (d/0 Diffuse)*; TAPPI Press: Atlanta, GA, USA, 2003; p. 9.
42. Kokaly, R.; Clark, R.; Swayze, G.; Livo, K.; Hoefen, T.; Pearson, N.; Wise, R.A.; Benzel, W.M.; Lowers, H.A.; Driscoll, R.L.; et al. *USGS Spectral Library Version 7*; US Geological Survey data release; United States Geological Survey (USGS): Reston, VA, USA, 2017.
43. Bowitz, J.; Ehling, A. Non-destructive infrared analyses: A method for provenance analyses of sandstones. *Environ. Earth Sci.* **2008**, *56*, 623–630. [CrossRef]